[27]W. G. Cady, *Piezoelectricity* (Dover, New York, 1964), p. 55. Note Eq. (6) is written in terms of the components of the strain tensor rather than in terms of conventional strains.
[28]C. Y. She, J. D. Masso, and D. F. Edwards, J. Phys. Chem. Solids **32**, 1887 (1971). Note that the values given in Table IV are the average of the observations made by these authors for phonon propagation at 45° to the optic axis.
[29]S. M. Shapiro and J. D. Axe, Phys. Rev. B **6**, 2420 (1972).
[30]J. F. Scott, Am. J. Phys. **39**, 1360 (1971).
[31]A. S. Pine and P. E. Tannenwald, Phys. Rev. **178**, 1424 (1969).
[32]J. F. Scott, Phys. Rev. Lett. **21**, 907 (1968).
[33]The elastic compliance constants used to evaluate the deformation potential constants were those of H. J. McSkimin, P. Andreatch, and R. N. Thurston [J. Appl. Phys. **36**, 1624 (1965)] at −195.8 °C. Note that this paper gives a positive sign for s_{14} resulting in opposite signs for c and d. Also, note that only the relative sign of c and d is determined by our measurements.
[34]See, for example, D. A. Kleinman and W. G. Spitzer, Phys. Rev. **125**, 16 (1962); M. E. Elcombe, Proc. Phys. Soc. Lond. **91**, 947 (1967); A. P. Mirgordskii, A. N. Lazarev, and I. P. Makarenko, Opt. Spektrosk. **29**, 539 (1970) [Opt. Spectrosc. **29**, 289 (1970)].
[35]S. Venugopalan and A. K. Ramdas, Bull. Am. Phys. Soc. **18**, 75 (1973).

PHYSICAL REVIEW B VOLUME 8, NUMBER 2 15 JULY 1973

Effect of Uniaxial Stress on the Raman Spectra of Cubic Crystals: CaF_2, BaF_2, and $Bi_{12}GeO_{20}$†

S. Venugopalan and A. K. Ramdas
Department of Physics, Purdue University, West Lafayette, Indiana 47907
(Received 12 February 1973)

The effect of uniaxial stress on the first-order Raman spectra of the cubic crystals, CaF_2, BaF_2, and $Bi_{12}GeO_{20}$ is studied at ≃15 °K using a quantitative-stress cryostat. Both CaF_2 and BaF_2 belong to the space group O_h^5 ($Fm3m$) and possess a single triply degenerate Raman-active zone-center optical phonon of F_{2g} symmetry. In contrast, $Bi_{12}GeO_{20}$ has a very rich first-order Raman spectrum consisting of lines *A*, *E*, *F*, and LO-TO-split *F* modes. The effect of uniaxial stress on the F_{2g} line of CaF_2 and on Raman lines typical of the different symmetries in $Bi_{12}GeO_{20}$ is studied up to 7 kbar with compressive force $\vec{F}$ along [001], [111] or [110]. The Raman line of BaF_2 is studied up to 2.4 kbar for $\vec{F}$ || [001]. The stress-induced splittings and polarization characteristics in each case can be understood on the basis of the reduced symmetry of the crystal under applied stress. Using a perturbing Hamiltonian linear in strain, the secular equation is derived for phonons of each symmetry in terms of phenomenological "deformation-potential constants." Phonons of *A*, *E*, and *F* symmetry in *T* and of F_{2g} symmetry in O_h are characterized by one, three, four, and three deformation-potential constants, respectively. Within the framework of this theory, the splittings as a function of the crystallographic orientation of the applied force can be correlated in terms of the deformation-potential constants, whereas the intensities of the stress-induced components can be calculated in terms of the zero-stress polarizability-tensor components. Experimentally, in all the cases the positions of the stress-induced components are observed to vary linearly with stress; the splittings, shifts, and polarization characteristics are consistent with the predictions based on the reduced symmetry of the crystal as well as the deformation-potential approach. On the basis of the observed polarization characteristics of the stress-induced components, appropriate eigenvalues have been associated with them and the deformation-potential constants have been obtained for all the lines studied.

I. INTRODUCTION

Uniaxial stress as an external perturbation has been successfully employed in solid-state spectroscopy[1]; optical spectra associated with localized electronic levels,[2] electronic band structure,[3] phonons,[4] and localized vibrations[5] have yielded significant information when studied under uniaxial stress. Recently piezospectroscopy has been applied in the study of Raman spectra associated with phonons in a number of crystals. It is interesting to note that the first example of a piezospectroscopic study is that of Marieé and Mathieu[6] who studied the Raman spectrum of α-quartz under uniaxial stress. However, the limitations of prelaser Raman spectroscopy prevented them from exploiting the full potential of the technique. Recently the Raman spectrum of α-quartz has been reexamined by Tekippe *et al.*[7]; in this work the use of low temperatures in conjunction with Ar^+-laser radiation as exciting source enabled the direct observation of stress-induced splittings and shifts of the Raman line. Anastassakis *et al.*[8] and Cerdeira *et al.*[9] have studied the first-order Raman spectra of Si, Ge, as well as III-V and II-VI compound semiconductors. These cubic crystals were investigated in the backscattering configuration using the reflection geometry at room temperature.

The purpose of this paper is to present the results of a low-temperature piezospectroscopic study

of the Raman spectra of CaF_2 and BaF_2[10] as well as several prominent Raman lines in the spectrum of $Bi_{12}GeO_{20}$ (BGO). All these crystals are cubic and transparent in the visible region. Both CaF_2 and BaF_2 belong to the space group $O_h^5(Fm3m)$ and possess a single Raman-active, triply degenerate zone-center optical phonon of F_{2g} symmetry.[11,12] In contrast, $Bi_{12}GeO_{20}$ which belongs to the space group $T^3(I23)$ has a very rich first-order Raman spectrum consisting of nondegenerate (A), doubly degenerate (E), triply degenerate (F), as well as LO-TO-split F modes.[13] Thus these crystals provide excellent examples for studying the effects of uniaxial stress on different types of phonons. The stress-induced splittings and shifts in the energies of the phonons are discussed on the basis of symmetry arguments and a perturbation theory using a phenomenological strain Hamiltonian.

II. EXPERIMENTAL PROCEDURE

Oriented single crystals of CaF_2 and BaF_2 of the highest purity available were obtained from Harshaw Chemical Co.[14] The $Bi_{12}GeO_{20}$ samples were cut from a single-crystal ingot of high optical quality supplied by Isomet Corp.[15] After orienting with x rays, rectangular parallelepiped samples with three orientations were obtained, their face normals being [100], [010], [001]; [1$\bar{1}$0], [001], [110]; and [11$\bar{2}$], [$\bar{1}$10], [111]. The samples were polished following the procedure described earlier.[13] The polished samples had typical dimensions of $5\times2.5\times1.25$ mm, the long dimension being the direction of compression. The ends of the sample were ground perpendicular to the length of the sample and glued into two copper cups. The method of mounting the sample and the low-temperature stress cryostat used in these studies have been described in detail elsewhere.[16] In this investigation the piezospectroscopic measurements were made with uniaxial compression.

The laser Raman spectrometer used in the present measurements has been described before.[13] As $Bi_{12}GeO_{20}$ has a rather high absorption[17,18] and optical rotatory power[18,19] for the lines of the Ar^+ laser, the 6328-Å radiation with ~100 mW of incident power was used to excite its Raman spectrum.[13] In contrast, both CaF_2 and BaF_2 are highly transparent in the entire visible region and thus the 4880-Å radiation with ~1.5 W was used for exciting their Raman spectra. The spectral resolution used in the study of $Bi_{12}GeO_{20}$ is ~0.5 cm^{-1} whereas it is ~0.8 cm^{-1} for the case of CaF_2 and BaF_2. In the study of $Bi_{12}GeO_{20}$, the depolarization effects arising from optical activity were minimized[13] by making the incident beam traverse the thickness of the crystal (~1.25 mm) within a depth of 1 mm from the scattering face.

In general, at low temperatures the half-width of Raman lines decreases. In addition, the peak intensity increases for most lines except those having a rather low frequency. Thus it is advantageous to perform high-resolution piezospectroscopic measurements at low temperatures. All the piezospectroscopic studies reported in this paper were performed using liquid helium as coolant and the temperature of the sample is estimated to be ~15 °K.

In order to measure accurately the position of the Raman line in CaF_2 the 4956.04- and 4965.04-Å emission lines from a potassium discharge lamp[20] were used as calibration lines. In the case of BaF_2, the 4944.83-Å line from a neodymium hollow-cathode lamp[21] served as the calibration line. The spectra reported here are uncorrected for the polarization and wavelength responses of the instrument. In polarization measurements it was noticed that the observed intensity was somewhat sensitive to the positioning of the analyzer. Owing to this factor and the very small slit widths used in these measurements, the observed intensities were reproducible only within ~20% with our experimental conditions. Hence the agreement of the observed intensities in all the spectra with the expected behavior is generally qualitative.

III. THEORY

In general uniaxial stress lowers the symmetry of a crystal; for a cubic crystal this is true for any direction of the applied force with respect to the crystallographic axes. The symmetry under stress can be deduced by retaining the symmetry elements common to both the strain ellipsoid and the initial symmetry of the crystal.[22] The irreducible representation corresponding to a given state in the unstressed crystal can be correlated to the irreducible representations of the new point group. The lifting of any degeneracy associated

TABLE I. Decomposition of the irreducible representation F_{2g} of O_h into the irreducible representations of the new point group in the presence of a uniaxial stress. The degeneracies of the representations are shown in parentheses.

Direction of compression	New point-group symmetry	$\vec{F}=0$	$\vec{F}\neq0$
[001]	D_{4h}	$F_{2g}(3)$	$B_{2g}(1)$ $E_g(2)$
[111]	D_{3d}	$F_{2g}(3)$	$A_{1g}(1)$ $E_g(2)$
[110]	D_{2h}	$F_{2g}(3)$	$A_g(1)$ $B_{2g}(1)$ $B_{3g}(1)$

TABLE II. Decomposition of the irreducible representations A, E, and F of T into the irreducible representations of the new point group in the presence of a uniaxial stress. The degeneracies of the representations are shown in parentheses.

Direction of compression	New point-group symmetry	A		E		F	
		$\vec{F}=0$	$\vec{F}\neq 0$	$\vec{F}=0$	$\vec{F}\neq 0$	$\vec{F}=0$	$\vec{F}\neq 0$
[001]	D_2	$A(1)$	$A(1)$	$E(2)$	$A(1)$	$F(3)$	$B_1(1)$
							$B_2(1)$
					$A(1)$		$B_3(1)$
[111]	C_3	$A(1)$	$A(1)$	$E(2)$	$E(2)$	$F(3)$	$A(1)$
							$E(2)$
[110]	C_2	$A(1)$	$A(1)$	$E(2)$	$A(1)$	$F(3)$	$A(1)$
					$A(1)$		$B(1)$

TABLE III. Polarizability-tensor components of the sublevels of the F_{2g} mode of O_h in the presence of a uniaxial stress: $\hat{x} \parallel [100]$, $\hat{y} \parallel [010]$, $\hat{z} \parallel [001]$; $\hat{x}' \parallel [\bar{1}10]$, $\hat{y}' \parallel [001]$, $\hat{z}' \parallel [110]$; $\hat{x}'' \parallel [11\bar{2}]$, $\hat{y}'' \parallel [\bar{1}10]$, $\hat{z}'' \parallel [111]$.

New point-group symmetry	Irreducible representation	Polarizability-tensor components
D_{4h}	B_{2g}	α_{xy}
	E_g	α_{yz}, α_{zx}
D_{3d}	A_{1g}	$\alpha_{x''x''}+\alpha_{y''y''}$, $\alpha_{z''z''}$
	E_g	$(\alpha_{x''x''}-\alpha_{y''y''}, \alpha_{x''y''})(\alpha_{y''z''}, \alpha_{z''x''})$
D_{2h}	A_g	$\alpha_{x'x'}$, $\alpha_{y'y'}$, $\alpha_{z'z'}$
	B_{2g}	$\alpha_{y'x'}$
	B_{3g}	$\alpha_{y'z'}$

with energy levels of the unstressed crystal follows in a straightforward manner from this procedure. Table I summarizes the decomposition of the F_{2g} representation of the point group O_h in the presence of a compressive force along [001], [111], or [110]. Table II gives similar information for the A, E, and F representations of the point group T. Since Raman lines originate from transitions between the totally symmetric ground state and the excited state having the irreducible representation of the phonon, the representation for the polarizability tensor must contain that of the phonon. Thus the polarizability-tensor elements associated with the stress-induced components are those which transform according to the appropriate representation of the new point group for a given component; these are summarized in Tables III and IV.

From the foregoing approach it is clear that symmetry arguments are very useful in deducing the behavior of a phonon both with regard to the removal of degeneracy and the polarization characteristics of the stress-induced components. However, group theory does not predict the magnitudes of the stress-induced splittings or shifts in the frequency of a phonon nor does it relate the intensities of the stress-induced components with that at zero stress. A perturbation calculation using a phenomenological Hamiltonian linear in strain has proved very useful[23,24] in this context. In this approach, the strain-induced potential is expressed in such a manner that each part of the potential transforms according to a particular irreducible representation of the point group of the crystal. Using basis functions appropriate to the irreducible representation of the energy level under consideration, one can obtain the secular equation in first-order perturbation theory. The potential and the basis functions have definite symmetry properties and thus the group-theoretical matrix-element theorem[25] can be exploited for determining the non-zero matrix elements. In addition, the independent matrix elements can be determined from the requirement that the matrix element remain invariant under symmetry operations of the point group. Thus the secular equation can be simplified and expressed in terms of the components of the strain tensor and the independent matrix elements or the "deformation-potential constants." The secular equation can be diagonalized for a given direction of uniaxial stress to yield the eigenvalues and eigenvectors. The eigenvalues give the stress-induced splittings in the energies of the phonons.[26] The eigenvectors in turn can be used to determine the linear combinations of the zero-stress polarizability tensors, which are appropriate for describing the polarization characteristics of the stress-induced components. Within the framework of this phenomenological theory, the splittings for different crystallographic orientations of the applied force can be correlated in terms of the deformation-potential constants, whereas the intensities of the stress-induced components can be calculated in terms of the zero-stress polarizability-tensor components.

In the linear approximation, the strain Hamil-

TABLE IV. Polarizability-tensor components of the sublevels of the A, E, and F modes of T in the presence of a uniaxial stress; the coordinate axes are the same as described in Table III.

New point-group symmetry	Irreducible representation	Polarizability-tensor components
D_2	A	α_{xx}, α_{yy}, α_{zz}
	B_1	α_{xy}
	B_2	α_{zx}
	B_3	α_{yz}
C_3	A	$\alpha_{x''x''}+\alpha_{y''y''}$, $\alpha_{z''z''}$
	E	$(\alpha_{x''x''}-\alpha_{y''y''}, \alpha_{x''y''})(\alpha_{y''z''}, \alpha_{z''x''})$
C_2	A	$\alpha_{x'x'}$, $\alpha_{y'y'}$, $\alpha_{z'z'}$, $\alpha_{x'z'}$
	B	$\alpha_{y'z'}$, $\alpha_{y'x'}$

tonian can be expressed as

$$V=\sum_{i,j} V_{ij}\epsilon_{ij}, \quad i,j=x,y,z \tag{1}$$

where $\{V_{ij}\}$ and $\{\epsilon_{ij}\}$ are symmetric second-rank tensors. V_{ij} is an operator which is a function of the coordinates.

A. F_{2g} Representation of Point Group O_h

We can rewrite Eq. (1) as

$$\begin{aligned} V=&\tfrac{1}{3}(V_{xx}+V_{yy}+V_{zz})(\epsilon_{xx}+\epsilon_{yy}+\epsilon_{zz})\\ &+\tfrac{1}{6}(2V_{zz}-V_{xx}-V_{yy})(2\epsilon_{zz}-\epsilon_{xx}-\epsilon_{yy})\\ &+\tfrac{1}{2}(V_{xx}-V_{yy})(\epsilon_{xx}-\epsilon_{yy})\\ &+2V_{yz}\epsilon_{yz}+2V_{zx}\epsilon_{zx}+2V_{xy}\epsilon_{xy}. \end{aligned} \tag{2}$$

In Eq. (2) the terms in the potential are regrouped such that $(V_{xx}+V_{yy}+V_{zz})$ transforms as A_{1g}, $(2V_{zz}-V_{xx}-V_{yy})$ and $(V_{xx}-V_{yy})$ as E_g, and V_{yz}, V_{zx}, and V_{xy} as F_{2g}; here x, y, and z are the cubic axes. The basis functions appropriate for the representations A_{1g}, E_g, and F_{2g} in O_h are listed in Table V. For calculating the matrix elements of V, we need the decomposition of products of the form $f_i f_j$ into the basis functions of O_h; $i,j=\xi,\eta,\zeta$. The decomposition of such products is given in Table VI. Using the matrix-element theorem and symmetry arguments, the secular equation can be expressed in terms of three deformation-potential constants a, b, and c as follows:

$$\begin{vmatrix} a\epsilon_{xx}+b(\epsilon_{yy}+\epsilon_{zz})-\lambda & 2c\epsilon_{xy} & 2c\epsilon_{zx} \\ 2c\epsilon_{xy} & a\epsilon_{yy}+b(\epsilon_{zz}+\epsilon_{xx})-\lambda & 2c\epsilon_{yz} \\ 2c\epsilon_{zx} & 2c\epsilon_{yz} & a\epsilon_{zz}+b(\epsilon_{xx}+\epsilon_{yy})-\lambda \end{vmatrix}=0, \tag{3}$$

where

$$\begin{aligned} a=&\tfrac{1}{9}\left(\langle f_0'|V_{xx}+V_{yy}+V_{zz}\rangle\right.\\ &\left.+\langle f_1'|2V_{zz}-V_{xx}-V_{yy}\rangle\right),\\ b=&\tfrac{1}{18}\left(2\langle f_0'|V_{xx}+V_{yy}+V_{zz}\rangle\right.\\ &\left.-\langle f_1'|2V_{zz}-V_{xx}-V_{yy}\rangle\right), \end{aligned}$$

$$c=\langle f_\xi'|V_{xy}\rangle=\langle f_\eta'|V_{zx}\rangle=\langle f_\zeta'|V_{yz}\rangle. \tag{4}$$

In cubic crystals, the components of the strain tensor $\{\epsilon_{ij}\}$ are related to the components of the stress tensor $\{\sigma_{ij}\}$ through the compliance constants s_{ij} as given in Eq. (5), when referred to the cubic axes[27]:

$$\begin{bmatrix}\epsilon_{xx}\\ \epsilon_{yy}\\ \epsilon_{zz}\\ \epsilon_{yz}\\ \epsilon_{zx}\\ \epsilon_{xy}\end{bmatrix}=\begin{bmatrix} s_{11} & s_{12} & s_{12} & 0 & 0 & 0\\ s_{12} & s_{11} & s_{12} & 0 & 0 & 0\\ s_{12} & s_{12} & s_{11} & 0 & 0 & 0\\ 0 & 0 & 0 & \frac{1}{2}s_{44} & 0 & 0\\ 0 & 0 & 0 & 0 & \frac{1}{2}s_{44} & 0\\ 0 & 0 & 0 & 0 & 0 & \frac{1}{2}s_{44}\end{bmatrix}\begin{bmatrix}\sigma_{xx}\\ \sigma_{yy}\\ \sigma_{zz}\\ \sigma_{yz}\\ \sigma_{zx}\\ \sigma_{xy}\end{bmatrix}. \tag{5}$$

Thus, for a given direction of uniaxial stress, the associated strain components can be determined and substituted in Eq. (3) and the eigenvalues and eigenvectors obtained by diagonalizing it.

From Eqs. (3) and (5) we can deduce the expressions for the energy shifts, which can be compared with experimental results for the applied force $\vec{F}$ along [001], [111], or [110]. The eigenvalues (λ) and eigenvectors (Λ) for these three cases are as follows:

$\vec{F}\parallel[00]$:

$$\lambda_1=\lambda_2=T[(a+b)s_{12}+bs_{11}]\equiv\lambda_D,$$

$$\lambda_3=T[as_{11}+2bs_{12}]\equiv\lambda_S,$$

$$\Lambda_D=\begin{bmatrix}1\\0\\0\end{bmatrix},\ \begin{bmatrix}0\\1\\0\end{bmatrix};\quad \Lambda_S=\begin{bmatrix}0\\0\\1\end{bmatrix}; \tag{6}$$

$\vec{F}\parallel[111]$:

$$\lambda_1=\lambda_2=\tfrac{1}{3}T[(a+2b)(s_{11}+2s_{12})-cs_{44}]\equiv\lambda_D,$$

TABLE V. Basis functions for A_{1g}, E_g, and F_{2g} representations of the point group O_h.

Irreducible representation	Basis function	
A_{1g}	$f_0 = X^2+Y^2+Z^2$,	$f_0' = X^2Y^2+Y^2Z^2+Z^2X^2$
E_g	$f_1 = 2Z^2-X^2-Y^2$, $f_2 = \sqrt{3}\,(X^2-Y^2)$,	$f_1' = 2X^2Y^2-Y^2Z^2-Z^2X^2$ $f_2' = \sqrt{3}\,(Y^2Z^2-Z^2X^2)$
F_{2g}	$f_\xi = YZ$, $f_\eta = ZX$, $f_\zeta = XY$,	$f_\xi' = X^2YZ$ $f_\eta' = Y^2ZX$ $f_\zeta' = Z^2XY$

$$\lambda_3 = \tfrac{1}{3}T[(a+2b)(s_{11}+2s_{12})+2cs_{44}] \equiv \lambda_S\,,$$

$$\Lambda_D = \frac{1}{\sqrt{6}}\begin{bmatrix}1\\1\\\bar{2}\end{bmatrix},\ \frac{1}{\sqrt{2}}\begin{bmatrix}\bar{1}\\1\\0\end{bmatrix};\quad \Lambda_S = \frac{1}{\sqrt{3}}\begin{bmatrix}1\\1\\1\end{bmatrix};\tag{7}$$

$\vec{F} \parallel [110]$:

$$\lambda_1 = T[(a+b)s_{12}+bs_{11}],$$

$$\lambda_2 = \tfrac{1}{2}T[a(s_{11}+s_{12})+b(s_{11}+3s_{12})+cs_{44}],$$

$$\lambda_3 = \tfrac{1}{2}T[a(s_{11}+s_{12})+b(s_{11}+3s_{12})-cs_{44}],$$

$$\Lambda_1 = \begin{bmatrix}0\\0\\1\end{bmatrix},\quad \Lambda_2 = \frac{1}{\sqrt{2}}\begin{bmatrix}1\\1\\0\end{bmatrix},\quad \Lambda_3 = \frac{1}{\sqrt{2}}\begin{bmatrix}\bar{1}\\1\\0\end{bmatrix}.\tag{8}$$

In the above T is the applied force per unit area and defined to be negative for compression; the subscripts D and S denote doublet and singlet, respectively.

It can be shown that any uniaxial stress can be expressed as the sum of a hydrostatic stress and a shear stress.[28] Thus the effect of a uniaxial stress on a degenerate level can be regarded as a hydrostatic shift of the energy level followed by a splitting due to the shear components of the stress. The eigenvalues in Eqs. (6)–(8) can thus be rewritten

$\vec{F} \parallel [001]$:

$$\lambda_S = \lambda_H + \tfrac{2}{3}\lambda_{[001]},\qquad \lambda_D = \lambda_H - \tfrac{1}{3}\lambda_{[001]},\tag{9}$$

where $\lambda_H = \frac{1}{3}T(a+2b)(s_{11}+2s_{12})$ and $\lambda_{[001]} = T(a-b)\times(s_{11}-s_{12})$;

$\vec{F} \parallel [111]$:

$$\lambda_S = \lambda_H + \tfrac{2}{3}\lambda_{[111]},\qquad \lambda_D = \lambda_H - \tfrac{1}{3}\lambda_{[111]},\tag{10}$$

where $\lambda_{[111]} = Tcs_{44}$;

$\vec{F} \parallel [110]$:

$$\lambda_1 = \lambda_H - \tfrac{1}{3}\lambda_{[001]},$$

$$\lambda_2 = \lambda_H + \tfrac{1}{6}\lambda_{[001]} + \tfrac{1}{2}\lambda_{[111]},$$

$$\lambda_3 = \lambda_H + \tfrac{1}{6}\lambda_{[001]} - \tfrac{1}{2}\lambda_{[111]}.\tag{11}$$

The polarizability tensors referred to the cubic axes for the F_{2g} mode in the unstressed crystal are

$$\begin{bmatrix}0&0&0\\0&0&d\\0&d&0\end{bmatrix},\ \begin{bmatrix}0&0&d\\0&0&0\\d&0&0\end{bmatrix},\ \begin{bmatrix}0&d&0\\d&0&0\\0&0&0\end{bmatrix}.\tag{12}$$

For uniaxial stress along a specified crystallographic direction, the eigenvectors of Eq. (3) can be used to determine the new linear combinations of the zero-stress tensors previously given. However, these linear combinations are still referred to the cubic axes and they must be transformed to the laboratory axes. The appropriate linear combinations transformed to the laboratory axes are given in Table VII for $\vec{F} \parallel [001]$, [111], or [110]. The system of axes as well as the eigenvector corresponding to each tensor is also given.

B. F Representation of Point Group T

The basis functions for A, E, and F representations are given in Table VIII. The decomposition of products of the form $\chi_i\chi_j$, where $i, j = \xi, \eta, \zeta$, into the basis functions of T is given in Table IX. It should be noted that the doubly degenerate representation is separably degenerate in the point group T.

The strain-induced potential given in Eq. (1) can be rewritten as follows:

$$\begin{aligned}V = {}& \tfrac{1}{3}(V_{xx}+V_{yy}+V_{zz})(\epsilon_{xx}+\epsilon_{yy}+\epsilon_{zz})\\ &+\tfrac{1}{3}(\omega^*V_{xx}+\omega V_{yy}+V_{zz})(\omega\epsilon_{xx}+\omega^*\epsilon_{yy}+\epsilon_{zz})\\ &+\tfrac{1}{3}(\omega V_{xx}+\omega^*V_{yy}+V_{zz})(\omega^*\epsilon_{xx}+\omega\epsilon_{yy}+\epsilon_{zz})\\ &+2V_{xy}\epsilon_{xy}+2V_{yz}\epsilon_{yz}+2V_{zx}\epsilon_{zx}.\end{aligned}\tag{13}$$

As discussed for the case of the F_{2g} representation in O_h, again one can write the secular equation in first-order degenerate perturbation theory for this case. Using Table IX, when the matrix-element theorem and symmetry arguments for the matrix

TABLE VI. Decomposition of the products f_if_j into the basis functions of O_h; $i, j = \xi, \eta, \zeta$.

f_i \ f_j	f_ξ	f_η	f_ζ
f_ξ	$\frac{1}{3}f_0' - \frac{1}{6}f_1' + \frac{1}{6}\sqrt{3}f_2'$	f_ζ'	f_η'
f_η	f_ζ'	$\frac{1}{3}f_0' - \frac{1}{6}f_1' - \frac{1}{6}\sqrt{3}f_2'$	f_ξ'
f_ζ	f_η'	f_ξ'	$\frac{1}{3}f_0' + \frac{1}{3}f_1'$

elements are applied to this case, it turns out that there are four independent matrix elements or deformation-potential constants denoted as a, b, c, and d. The secular equation can be written as

$$\begin{vmatrix} a\epsilon_{xx}+b(\epsilon_{yy}+\epsilon_{zz}) & 2c\epsilon_{xy} & 2c\epsilon_{zx} \\ +d(\epsilon_{zz}-\epsilon_{yy})-\lambda & & \\ 2c\epsilon_{xy} & a\epsilon_{yy}+b(\epsilon_{zz}+\epsilon_{xx}) & 2c\epsilon_{yz} \\ & +d(\epsilon_{xx}-\epsilon_{zz})-\lambda & \\ 2c\epsilon_{zx} & 2c\epsilon_{yz} & a\epsilon_{zz}+b(\epsilon_{xx}+\epsilon_{yy}) \\ & & +d(\epsilon_{yy}-\epsilon_{xx})-\lambda \end{vmatrix} = 0 , \tag{14}$$

where

$$a = \tfrac{1}{9}(\langle\chi_0|V_{xx}+V_{yy}+V_{zz}\rangle + \langle\chi_1|\omega^* V_{xx}+\omega V_{yy}+V_{zz}\rangle + \langle\chi_2|\omega V_{xx}+\omega^* V_{yy}+V_{zz}\rangle),$$

$$b = \tfrac{1}{18}(2\langle\chi_0|V_{xx}+V_{yy}+V_{zz}\rangle - \langle\chi_1|\omega^* V_{xx}+\omega V_{yy}+V_{zz}\rangle - \langle\chi_2|\omega V_{xx}+\omega^* V_{yy}+V_{zz}\rangle), \tag{15}$$

$$c = \langle\chi_\xi'|V_{xy}\rangle = \langle\chi_\eta'|V_{zx}\rangle = \langle\chi_\zeta'|V_{yz}\rangle ,$$

$$d = -(i/6\sqrt{3})(\langle\chi_1|\omega^* V_{xx}+\omega V_{yy}+V_{zz}\rangle - \langle\chi_2|\omega V_{xx}+\omega^* V_{yy}+V_{zz}\rangle).$$

It is worth noting here that when $d=0$, Eq. (14) reduces to Eq. (3). Equation (14) can be diagonalized for $\vec{F}\parallel[001]$, [111], or [110], the ϵ_{ij}'s being obtained from Eq. (5) for a given direction of uniaxial stress. Again the effect of a uniaxial stress can be regarded as comprised of a hydrostatic shift of the energy level followed by a splitting due to the shear components of the stress.

For $\vec{F}\parallel[001]$, Eq. (14) yields three distinct eigenvalues and their associated eigenvectors, viz.,

$$\lambda_1 = \lambda_H - \tfrac{1}{3}\lambda_{[001]} + \lambda_d ,$$
$$\lambda_2 = \lambda_H - \tfrac{1}{3}\lambda_{[001]} - \lambda_d ,$$
$$\lambda_3 = \lambda_H + \tfrac{2}{3}\lambda_{[001]} , \tag{16}$$
$$\Lambda_1 = \begin{bmatrix}1\\0\\0\end{bmatrix}, \quad \Lambda_2 = \begin{bmatrix}0\\1\\0\end{bmatrix}, \quad \Lambda_3 = \begin{bmatrix}0\\0\\1\end{bmatrix} .$$

Here $\lambda_d = Td(s_{11}-s_{12})$; λ_H and $\lambda_{[001]}$ have the same form as in Eq. (9). Thus we see that for $\vec{F}\parallel[001]$ the degeneracy of the F mode is completely removed, whereas the F_{2g} mode in O_h splits into a doublet and a singlet. This is a consequence of the fourth deformation-potential constant d in this case.

For $\vec{F}\parallel[111]$, the eigenvectors and the form of the expressions for the eigenvalues of Eq. (14) are identical to those given in Eqs. (7) and (10) for the F_{2g} mode in O_h. For $\vec{F}\parallel[110]$, the degeneracy of

TABLE VII. Polarizability tensors of the sublevels of the F_{2g} mode of O_h, for $\vec{F}\parallel[001]$, [110], or [111]. The tensors are referred to the coordinate axes indicated in each case. The eigenvector corresponding to each tensor is also given.

$\vec{F}\parallel[001]$		$\vec{F}\parallel[110]$		$\vec{F}\parallel[111]$	
$\hat{x}\parallel[100]$, $\hat{y}\parallel[010]$, $\hat{z}\parallel[001]$		$\hat{x}'\parallel[\bar{1}10]$, $\hat{y}'\parallel[001]$, $\hat{z}'\parallel[110]$		$\hat{x}''\parallel[11\bar{2}]$, $\hat{y}''\parallel[\bar{1}10]$, $\hat{z}''\parallel[111]$	
Eigenvector	Polarizability tensor	Eigenvector	Polarizability tensor	Eigenvector	Polarizability tensor
$\begin{bmatrix}1\\0\\0\end{bmatrix}$	$\begin{bmatrix}0&0&0\\0&0&d\\0&d&0\end{bmatrix}$	$\frac{1}{\sqrt{2}}\begin{bmatrix}\bar{1}\\1\\0\end{bmatrix}$	$\begin{bmatrix}0&-d&0\\-d&0&0\\0&0&0\end{bmatrix}$	$\frac{1}{\sqrt{6}}\begin{bmatrix}1\\1\\\bar{2}\end{bmatrix}$	$\begin{bmatrix}-2d/\sqrt{6}&0&-d/\sqrt{3}\\0&2d/\sqrt{6}&0\\-d/\sqrt{3}&0&0\end{bmatrix}$
$\begin{bmatrix}0\\1\\0\end{bmatrix}$	$\begin{bmatrix}0&0&d\\0&0&0\\d&0&0\end{bmatrix}$	$\begin{bmatrix}0\\0\\1\end{bmatrix}$	$\begin{bmatrix}-d&0&0\\0&0&0\\0&0&d\end{bmatrix}$	$\frac{1}{\sqrt{2}}\begin{bmatrix}\bar{1}\\1\\0\end{bmatrix}$	$\begin{bmatrix}0&2d/\sqrt{6}&0\\2d/\sqrt{6}&0&-d/\sqrt{3}\\0&-d/\sqrt{3}&0\end{bmatrix}$
$\begin{bmatrix}0\\0\\1\end{bmatrix}$	$\begin{bmatrix}0&d&0\\d&0&0\\0&0&0\end{bmatrix}$	$\frac{1}{\sqrt{2}}\begin{bmatrix}1\\1\\0\end{bmatrix}$	$\begin{bmatrix}0&0&0\\0&0&d\\0&d&0\end{bmatrix}$	$\frac{1}{\sqrt{3}}\begin{bmatrix}1\\1\\1\end{bmatrix}$	$\begin{bmatrix}-d/\sqrt{3}&0&0\\0&-d/\sqrt{3}&0\\0&0&2d/\sqrt{3}\end{bmatrix}$

TABLE VIII. Basis functions for A, E, and F representations of the point group T; $\omega = e^{2\pi i/3}$.

Irreducible representation	Basis function
A	$\chi_0 = X^2 + Y^2 + Z^2$
$E\begin{cases} E_1 \\ E_2 \end{cases}$	$\chi_1 = \omega^* X^2 + \omega Y^2 + Z^2$ $\chi_2 = \omega X^2 + \omega^* Y^2 + Z^2$
F	$\chi_\xi = X$, $\chi_\xi' = YZ$ $\chi_\eta = Y$, $\chi_\eta' = ZX$ $\chi_\zeta = Z$, $\chi_\zeta' = XY$

the F mode is completely removed and the eigenvalues and eigenvectors are

$$\lambda_1 = \lambda_H - \tfrac{1}{3}\lambda_{[001]},$$
$$\lambda_2 = \lambda_H + \tfrac{1}{6}\lambda_{[001]} + \tfrac{1}{2}(\lambda_d^2 + \lambda_{[111]}^2)^{1/2},$$
$$\lambda_3 = \lambda_H + \tfrac{1}{6}\lambda_{[001]} - \tfrac{1}{2}(\lambda_d^2 + \lambda_{[111]}^2)^{1/2},$$
$$\Lambda_1 = \begin{bmatrix} 0 \\ 0 \\ 1 \end{bmatrix}, \quad \Lambda_2 = \frac{1}{(1+\alpha^2)^{1/2}} \begin{bmatrix} 1 \\ \alpha \\ 0 \end{bmatrix}, \tag{17}$$
$$\Lambda_3 = \frac{1}{(1+\alpha^2)^{1/2}} \begin{bmatrix} \bar{\alpha} \\ 1 \\ 0 \end{bmatrix},$$

where

$$\alpha = \frac{\lambda_{[111]}}{(\lambda_d^2 + \lambda_{[111]}^2)^{1/2} - \lambda_d}.$$

It may be noted here that if $\lambda_d \ll \lambda_{[111]}$, λ_2 and λ_3 in Eqs. (17) reduce to the same form as in Eqs. (11).

As the zero-stress polarizability tensors referred to the cubic axes for the F mode are identical to those in Eqs. (12), the new linear combinations of the polarizability tensors transformed to the laboratory axes for $\vec{F} \parallel [001]$ or $[111]$ are seen to be identical to those in Table VII. However, for $\vec{F} \parallel [110]$, the tensors will be different from those in Table VII if $\alpha \neq 1$; these are given in Table X.

As the F modes are simultaneously infrared active, long-range polarization fields are expected to split them into longitudinal-optic (LO) and transverse-optic (TO) phonons, with the former at a higher frequency.[29] In the right-angle scattering geometry employed in the present study, the direction of the applied force is perpendicular to the scattering plane which contains the phonon wave vector. Thus the zero-stress polarization directions of one of the TO components, $(TO)_\perp$, and the LO phonon lie in the scattering plane at right angles to each other and to the direction of applied force, whereas the polarization of the other TO component, $(TO)_\parallel$, is parallel to the applied force. The subscripts $\perp$ and $\parallel$ denote components with polarization perpendicular and parallel to the direction of force, respectively.

For $\vec{F} \parallel [111]$, the zero-stress polarization directions of $(TO)_\perp$ and LO are appropriate linear combinations of the eigenvectors of the doublet in Eq. (7), while the zero-stress polarization of $(TO)_\parallel$ is the eigenvector of the singlet. Thus we note that the zero-stress polarization directions of $(TO)_\parallel$, $(TO)_\perp$, and LO are compatible with the eigenvectors in the presence of the applied force along [111]. However, for $\vec{F} \parallel [001]$ or $[110]$ and the corresponding phonon wave vectors used in the experiment, the zero-stress polarization directions are no longer compatible with the eigenvectors in Eqs. (16) or (17), respectively, with the exception of $(TO)_\parallel$ for $\vec{F} \parallel [001]$.

For $\vec{F} \parallel [001]$ or $[110]$, it is seen from Eqs. (16) and (17) that the triply degenerate F mode is expected to split into three components. Thus in the case of LO-TO-split F mode, we expect the TO

TABLE IX. Decomposition of the products $\chi_i \chi_j$ into the basis functions of T; $i, j = \xi, \eta, \zeta$.

χ_i \ χ_j	χ_ξ	χ_η	χ_ζ
χ_ξ	$\frac{1}{3}(\chi_0 + \omega\chi_1 + \omega^*\chi_2)$	χ_ζ'	χ_η'
χ_η	χ_ζ'	$\frac{1}{3}(\chi_0 + \omega^*\chi_1 + \omega\chi_2)$	χ_ξ'
χ_ζ	χ_η'	χ_ξ'	$\frac{1}{3}(\chi_0 + \chi_1 + \chi_2)$

TABLE X. Polarizability tensors of the stress-induced components of the F mode of T, for $\vec{F} \parallel [110]$. The tensors are referred to the coordinate axes indicated. The eigenvector corresponding to each tensor is also given. $\gamma = (1-\alpha)/[2(1+\alpha^2)]^{1/2}$, $\rho = (1+\alpha)/[2(1+\alpha^2)]^{1/2}$.

$\vec{F} \parallel [110]$
$\hat{x}' \parallel [\bar{1}10]$, $\hat{y}' \parallel [001]$, $\hat{z}' \parallel [110]$

Eigenvector	Polarizability tensor
$\frac{1}{[1+\alpha^2]^{1/2}} \begin{bmatrix} \bar{\alpha} \\ 1 \\ 0 \end{bmatrix}$	$\begin{bmatrix} 0 & -\rho d & 0 \\ -\rho d & 0 & \gamma d \\ 0 & \gamma d & 0 \end{bmatrix}$
$\begin{bmatrix} 0 \\ 0 \\ 1 \end{bmatrix}$	$\begin{bmatrix} -d & 0 & 0 \\ 0 & 0 & 0 \\ 0 & 0 & d \end{bmatrix}$
$\frac{1}{[1+\alpha^2]^{1/2}} \begin{bmatrix} 1 \\ \alpha \\ 0 \end{bmatrix}$	$\begin{bmatrix} 0 & \gamma d & 0 \\ \gamma d & 0 & \rho d \\ 0 & \rho d & 0 \end{bmatrix}$

mode to split into two components for either direction of applied force. For $\vec{F} \parallel [111]$, we note from Eq. (7) that the stress-induced shift for the components polarized parallel to [111] is different from those for the components polarized in a perpendicular direction. Hence we again expect the TO mode to split into two components. Thus, for all three directions of applied force one expects the degeneracy of the TO mode to be removed while the LO mode shifts under the stress. Furthermore, when the magnitude of LO-TO splitting is independent of applied stress,[30] in the case of $\vec{F} \parallel [111]$ the rate of shift as a function of applied stress would be the same for $(TO)_\perp$ and LO while $(TO)_\parallel$ would exhibit a different rate of shift. In the absence of stress-dependent LO-TO splitting, the observed polarization characteristics of the LO-TO modes for $\vec{F} \neq 0$ can be used for assigning each component the appropriate eigenvalue from Eqs. (10), (16), or (17) for a given direction of the force; hence the deformation-potential constants of the LO-TO split F mode can be determined on this basis.

C. E Representation of Point Group T

The secular equation can be written down for the E representation of T using Eq. (13) and the basis functions for the E representation given in Table VIII. Simplification of the secular equation as described earlier shows that there exist three deformation-potential constants in this case, a real quantity designated as e and the other two being the real and an imaginary part of a complex quantity $u+iv=f$. The secular equation is

$$\begin{vmatrix} e(\epsilon_{xx}+\epsilon_{yy}+\epsilon_{zz})-\lambda & f(\omega^*\epsilon_{xx}+\omega\epsilon_{yy}+\epsilon_{zz}) \\ f^*(\omega\epsilon_{xx}+\omega^*\epsilon_{yy}+\epsilon_{zz}) & e(\epsilon_{xx}+\epsilon_{yy}+\epsilon_{zz})-\lambda \end{vmatrix} = 0 , \tag{18}$$

where

$$\begin{aligned} e &= \tfrac{1}{3}\langle \chi_1 | V_{xx}+V_{yy}+V_{zz} | \chi_1 \rangle , \\ f &= \tfrac{1}{3}\langle \chi_1 | \omega V_{xx}+\omega^* V_{yy}+V_{zz} | \chi_2 \rangle . \end{aligned} \tag{19}$$

Setting $\lambda_H = eT(s_{11}+2s_{12})$ and $\lambda_E = |f| T(s_{11}-s_{12})$, the eigenvalues and eigenvectors are given by

$\vec{F} \parallel [001]$:

$$\lambda_1 = \lambda_H + \lambda_E ,$$

$$\lambda_2 = \lambda_H - \lambda_E ,$$

$$\Lambda_1 = \frac{1}{\sqrt{2}}\begin{bmatrix} 1 \\ f^*/|f| \end{bmatrix}, \quad \Lambda_2 = \frac{1}{\sqrt{2}}\begin{bmatrix} 1 \\ -f^*/|f| \end{bmatrix} ; \tag{20}$$

$\vec{F} \parallel [110]$:

$$\lambda_1 = \lambda_H + \tfrac{1}{2}\lambda_E ,$$

$$\lambda_2 = \lambda_H - \tfrac{1}{2}\lambda_E ,$$

$$\Lambda_1 = \frac{1}{\sqrt{2}}\begin{bmatrix} 1 \\ -f^*/|f| \end{bmatrix}, \quad \Lambda_2 = \frac{1}{\sqrt{2}}\begin{bmatrix} 1 \\ f^*/|f| \end{bmatrix} . \tag{21}$$

It should be noted that the eigenvectors Λ_1 and Λ_2 in Eqs. (21) are interchanged compared to Eqs. (20). For $\vec{F} \parallel [111]$, $\lambda_1 = \lambda_2 = \lambda_H$ and hence the degeneracy of the E mode is not removed.

From Eqs. (20) and (21) we note that the magnitude of the stress-induced splitting for the E mode is $2\lambda_E$ for $\vec{F} \parallel [001]$, whereas it is λ_E for $\vec{F} \parallel [110]$. In addition, it should be noted that experimental results for the positions of the stress-induced components in either of the two cases enable the determination of the deformation-potential constant e and $|f|$. We demonstrate in the following that from the relative intensities of the stress-induced components, the real part u of the complex quantity f can be determined. Thus knowing $|f|$ and u, the *magnitude* of the imaginary part v can be determined in turn.

The zero-stress polarizability tensors for the E modes are given as

$$k\begin{bmatrix} \omega^* & 0 & 0 \\ 0 & \omega & 0 \\ 0 & 0 & 1 \end{bmatrix}, \quad k\begin{bmatrix} \omega & 0 & 0 \\ 0 & \omega^* & 0 \\ 0 & 0 & 1 \end{bmatrix} . \tag{22}$$

From the eigenvectors in Eqs. (20) and (21) the proper linear combinations of the above tensors can be determined for $\vec{F} \parallel [001]$ or [110] and they can be transformed to the laboratory axes. These are given in Table XI. From these tensors we can deduce the ratio of the intensities for the stress-induced components in the two experimental geometries employed here, viz., $x(zz+zx)y$ polarization or $x'(z'z'+z'x')y'$ polarization. For $\vec{F} \parallel [001]$,

$$\frac{I^{(1)}_{(zz+zx)}}{I^{(2)}_{(zz+zx)}} = \frac{|f|+u}{|f|-u} , \tag{23}$$

whereas, for $\vec{F} \parallel [110]$,

$$\frac{I^{(1)}_{(z'z'+z'x')}}{I^{(2)}_{(z'z'+z'x')}} = \frac{2|f|+u}{2|f|-u} , \tag{24}$$

where the superscripts 1 and 2 refer to eigenvalues λ_1 and λ_2, respectively, for each direction of applied force.

From Eqs. (23) and (24) we note that within the approximation the zero-stress intensity of the line is redistributed in the two stress-induced components, the ratio of their intensities can be used to determine u. Another conclusion derived from Eqs. (23) and (24) is that when $u \neq 0$, the pattern of relative intensities corresponding to λ_1 and λ_2 should be similar for $\vec{F} \parallel [001]$ and [110].

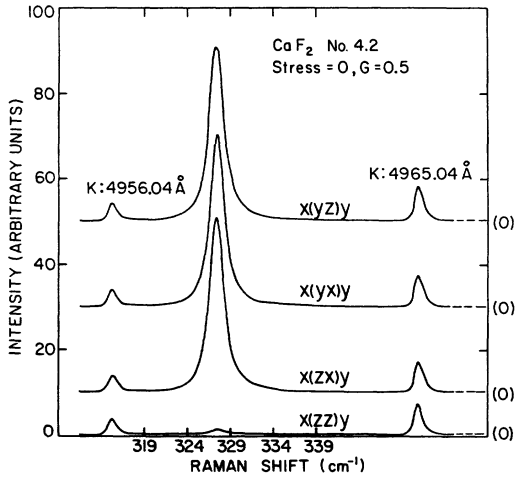

FIG. 1. Zero-stress Raman spectrum of CaF_2 and its polarization characteristics; $T \sim 15$ °K. The gain $G = 0.5$ corresponds to 2000 counts/sec for full scale deflection on the ratemeter. $\hat{x} \parallel [100]$, $\hat{y} \parallel [010]$, and $\hat{z} \parallel [001]$. On either side of the Raman line are calibration lines from a potassium discharge lamp.

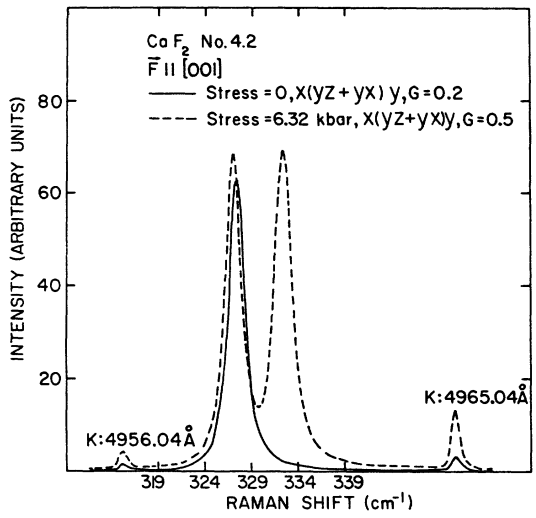

FIG. 2. Raman spectrum of CaF_2 for $\hat{F} \parallel [001]$; $T \sim 15$ °K. Note the change in relative gain between the zero-stress spectrum and that under applied stress. $\hat{x} \parallel [100]$, $\hat{y} \parallel [010]$, $\hat{z} \parallel [001]$.

D. *A* Representation of Point Group *T*

As the A modes are nondegenerate, their shift in energy as a function of the crystallographic direction of the applied force is isotropic and is given by

$$\lambda = gT(s_{11} + 2s_{12}), \tag{25}$$

where

$$g = \tfrac{1}{3}\langle \chi_0 | V_{xx} + V_{yy} + V_{zz} | \chi_0 \rangle .$$

IV. EXPERIMENTAL RESULTS AND DISCUSSION

A. Calcium Fluoride

At room temperature the triply degenerate F_{2g} zone-center phonon of CaF_2 occurs[11] at ~ 321 cm^{-1}. In the present study, at room temperature the Raman line was observed at 321.3 ± 0.5 cm^{-1} with a half-width of ~ 7.5 cm^{-1}. At ~ 15 °K, using the calibration lines from a potassium discharge lamp, the position of the Raman line was determined to be 327.3 ± 0.1 cm^{-1}, with a half-width of 2.0 cm^{-1}. Furthermore, it was observed that at 77 °K the position of the line did not change as compared to that at 15 °K. Srivastava *et al.*[12] determined the position of the Raman line of CaF_2 at 77 °K to be 330 ± 2 cm^{-1}, which is in fair agreement with our value.

Figure 1 shows the first-order Raman spectrum of CaF_2 at ~ 15 °K recorded with different polarization parameters. As expected from the polarizability tensors for the F_{2g} mode in Eq. (12), the intensities of the $x(yz)y$, $x(yx)y$, and $x(zx)y$ spectra are all nonzero, whereas the intensity corresponding to the diagonal component $x(zz)y$ is vanishingly small. Also, the three spectra corresponding to off-diagonal polarizability components are expected to yield equal intensity. The observed in-

TABLE XI. Polarizability tensors of the sublevels of the E mode of T, for $\hat{F} \parallel [001]$ or $[110]$. The tensors are referred to the coordinate axes indicated in each case. The eigenvector corresponding to each tensor is also given; $f^*/|f| = \beta$.

Eigenvector	$\hat{F} \parallel [001]$ $\hat{x} \parallel [100]$, $\hat{y} \parallel [010]$, $\hat{z} \parallel [001]$	$\hat{F} \parallel [110]$ $\hat{x}' \parallel [\bar{1}10]$, $\hat{y}' \parallel [001]$, $\hat{z}' \parallel [110]$
$\frac{1}{\sqrt{2}}\begin{bmatrix}1\\ \beta\end{bmatrix}$	$\frac{k}{\sqrt{2}}\begin{bmatrix}\omega^*+\beta\omega & 0 & 0\\ 0 & \omega+\beta\omega^* & 0\\ 0 & 0 & (1+\beta)\end{bmatrix}$	$\frac{k}{\sqrt{2}}\begin{bmatrix}-\frac{1}{2}(1-\beta) & 0 & i\frac{1}{2}\sqrt{3}\,(1+\beta)\\ 0 & (1-\beta) & 0\\ i\frac{1}{2}\sqrt{3}\,(1+\beta) & 0 & -\frac{1}{2}(1-\beta)\end{bmatrix}$
$\frac{1}{\sqrt{2}}\begin{bmatrix}1\\ -\beta\end{bmatrix}$	$\frac{k}{\sqrt{2}}\begin{bmatrix}\omega^*-\beta\omega & 0 & 0\\ 0 & \omega-\beta\omega^* & 0\\ 0 & 0 & (1-\beta)\end{bmatrix}$	$\frac{k}{\sqrt{2}}\begin{bmatrix}-\frac{1}{2}(1+\beta) & 0 & i\frac{1}{2}\sqrt{3}\,(1-\beta)\\ 0 & (1+\beta) & 0\\ i\frac{1}{2}\sqrt{3}(1-\beta) & 0 & -\frac{1}{2}(1+\beta)\end{bmatrix}$

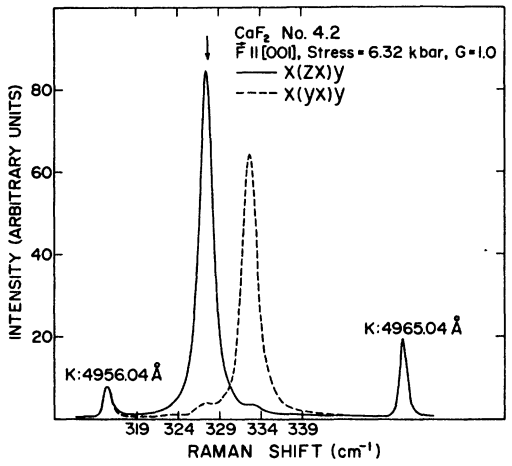

FIG. 3. Polarization characteristics of the stress-induced components in CaF_2 for $\vec{F} \parallel [001]$, at a stress of 6.32 kbar; $T \sim 15$ °K. The arrow denotes the zero-stress position of the line. $\hat{x} \parallel [100]$, $\hat{y} \parallel [010]$, $\hat{z} \parallel [001]$.

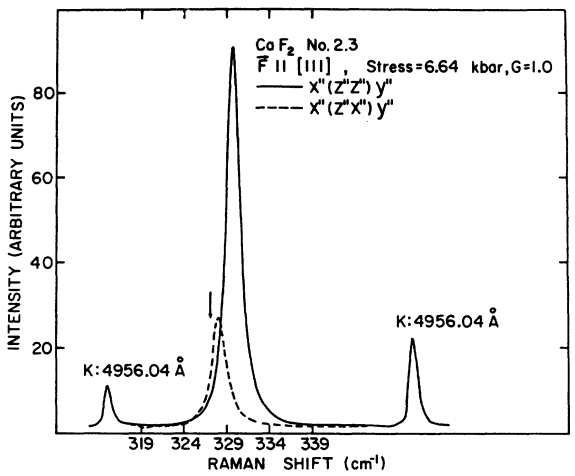

FIG. 5. Polarization characteristics of the stress-induced components in CaF_2 for $\vec{F} \parallel [111]$, at a stress of 6.64 kbar; $T \sim 15$ °K. The arrow denotes the zero-stress position of the line. $\hat{x}'' \parallel [\bar{1}10]$, $\hat{y}'' \parallel [11\bar{2}]$, $\hat{z}'' \parallel [111]$.

tensities are in qualitative agreement with this expectation. Thus we conclude that the Raman-active zone-center phonon in CaF_2 belongs to the F_{2g} symmetry as expected.[11]

It was pointed out in Sec. III that for $\vec{F} \parallel [001]$ the F_{2g} line is expected to split into a singlet and a doublet. In Fig. 2 the Raman spectrum of CaF_2 is shown in $x(yz+yx)y$ polarization for $\vec{F} \parallel [001]$. The zero-stress spectrum is also shown in the same polarization, for comparison. One clearly sees two stress-induced components with a splitting of ~ 6.0 cm^{-1}. The polarization features of the two components are shown in Fig. 3. The component at the higher frequency is observed in the $x(yx)y$ polarization, whereas the component which shifts very little from the zero-stress position denoted by the arrow is observed in the $x(zx)y$ polarization. It should be noted that these polarizations are consistent with those predicted in Table III for B_{2g} and E_g symmetries, respectively, in the new point group D_{4h}. In addition, these are in agreement with the predicted polarization characteristics for singlet and doublet, respectively, as seen from Table VII. The observed intensities for singlet and doublet are in qualitative agreement with the predictions from Table VII.

Figure 4 shows the stress-induced components for $\vec{F} \parallel [111]$. Again, the F_{2g} line splits into two components. The spectrum under applied stress

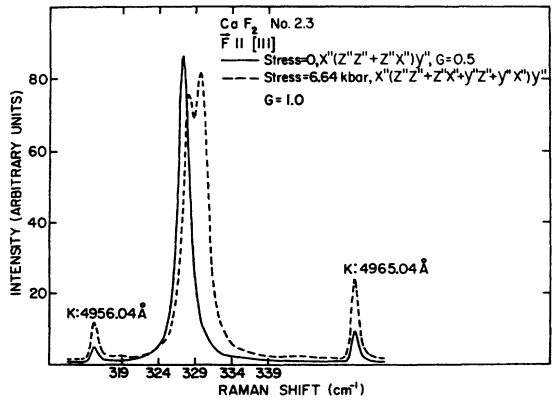

FIG. 4. Raman spectrum of CaF_2 for $\vec{F} \parallel [111]$; $T \sim 15$ °K. The spectrum under applied stress was recorded with incident light which had polarization components along z'' as well as y''. $\hat{x}'' \parallel [\bar{1}10]$, $\hat{y}'' \parallel [11\bar{2}]$, $z'' \parallel [111]$.

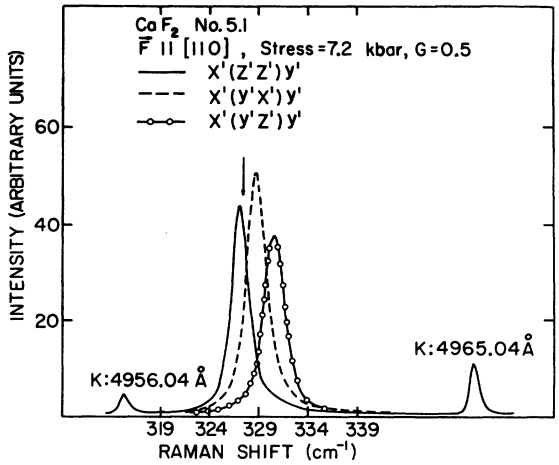

FIG. 6. Polarization characteristics of the stress-induced components in CaF_2 for $\vec{F} \parallel [110]$; at a stress of 7.2 kbar; $T \sim 15$ °K. The arrow denotes the zero-stress position of the line. $\hat{x}' \parallel [\bar{1}10]$, $\hat{y}' \parallel [001]$, $\hat{z}' \parallel [110]$.

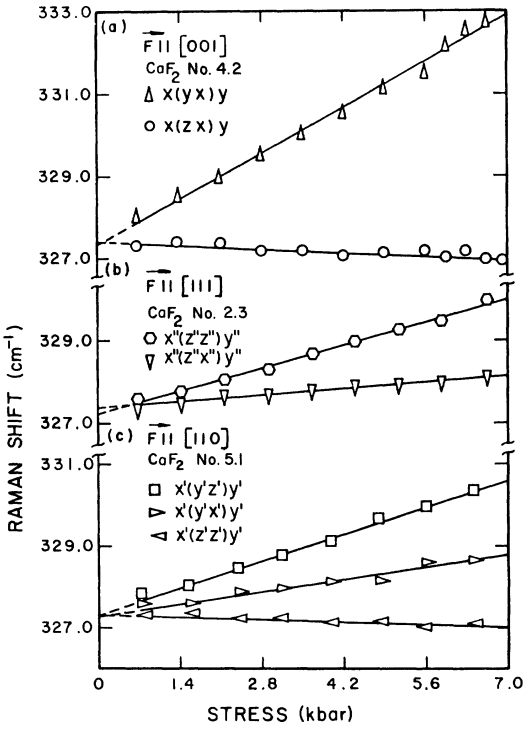

FIG. 7. Positions of the stress-induced components in CaF_2, as a function of the applied stress: (a) $\vec{F} \parallel [001]$, (b) $\vec{F} \parallel [111]$, (c) $\vec{F} \parallel [110]$. The straight lines represent linear least-squares fits to the data points in each case. Their slope as well as intercept at zero stress are plotted as given by the least-squares fit. Hence the intersections of the lines at small nonzero-stress values rather than at zero stress reflects the error in the calculated values of the stress. $\hat{x} \parallel [100]$, $\hat{y} \parallel [010]$, $\hat{z} \parallel [001]$; $\hat{x}' \parallel [\bar{1}10]$, $\hat{y}' \parallel [001]$, $\hat{z}' \parallel [110]$; $\hat{x}'' \parallel [\bar{1}10]$, $\hat{y}'' \parallel [11\bar{2}]$, $\hat{z}'' \parallel [111]$.

was obtained in this case with incident light which had polarization components along z'' as well as y'' directions. The quartz crystal used for rotating the polarization of incident light from z'' to y'' was tilted at an angle with respect to the laser beam. The angle of tilt was adjusted until the relative intensities of the stress-induced components were nearly equal. This enabled a clear observation of the two stress-induced components without isolating them on the basis of their polarization features. The polarization characteristics of the two components are shown in Fig. 5. From the polarization characteristics predicted in Tables III and VII, it is clear that the higher-frequency component seen in $x''(z''z'')y''$ polarization is the singlet and has the A_{1g} symmetry in D_{3d}. The lower-frequency component is seen in $x''(z''x'')y''$ and hence is the doublet which has the E_g symmetry in D_{3d}. From Table VII, we see that the intensity of the $x''(z''z'')y''$ spectrum must be four times larger than that of the $x''(z''x'')y''$ polarization; the observed intensities are in qualitative agreement with this expectation.

Both from the perturbation theory and group-theoretical correlation, it was shown that the degeneracy of the F_{2g} mode should be completely lifted for $\vec{F} \parallel [110]$. Figure 6 shows the experimental results for this direction of compressive force. Clearly, three distinct components are seen and their observed polarization characteristics are in agreement with those predicted in Tables III and VII. From Table III we note that the component with $x'(y'z')y'$ polarization belongs to B_{3g} symmetry in the new point group D_{2h}, while those with $x'(y'x')y'$ and $x'(z'z')y'$ belong to B_{2g} and A_g, respectively. From Table VII we note that the intensities in all three polarizations should be equal; the observed intensities are in fair agreement with this prediction.

Within the deformation-potential approach discussed earlier, the energy shifts for the stress-induced components are expected to be linear in T. Figure 7 shows the linear least-squares fit of the positions of the stress-induced components as a function of the magnitude of applied stress in the case of CaF_2, for $\vec{F} \parallel [001]$, [111], or [110]. It is seen that the experimental points in each case do exhibit a linear behavior rather closely. The least-squares fit for a given measurement generally yielded probable errors of 2–4% in the slopes for components which exhibit a considerable shift as a function of applied stress. However, for components which undergo little shift from the zero-stress position of the line even at the highest stress, e.g., $x(zx)y$ or $x'(z'z')y'$, the probable errors were 10–15%. In addition, for a given stress the hydrostatic shift λ_H showed a variation of 10–15% within the three directions of applied force considered here. Thus our experience in this case as well as in the piezospectroscopic study of α-quartz[7] indicates that the slopes of the lines as in Fig. 7 are reproducible to within 15%, and hence the deformation-potential constants deduced from the slopes are accurate to within 15%.

From Eqs. (6) and (7) we note that given the compliance constants of CaF_2[31] the three deformation-potential constants a, b, and c associated with the F_{2g} mode can be obtained from the two measurements with $\vec{F} \parallel [001]$ and $\vec{F} \parallel [111]$. Hence the slopes of the three stress-induced components for $\vec{F} \parallel [110]$, which are determined by Eq. (8), can be predicted and these values when compared with the experiment for $\vec{F} \parallel [110]$ serve as an internal check for consistency. Such a check showed that the agreement was very good. The deformation-potential constants of the F_{2g} mode of CaF_2 are listed in Table XII.

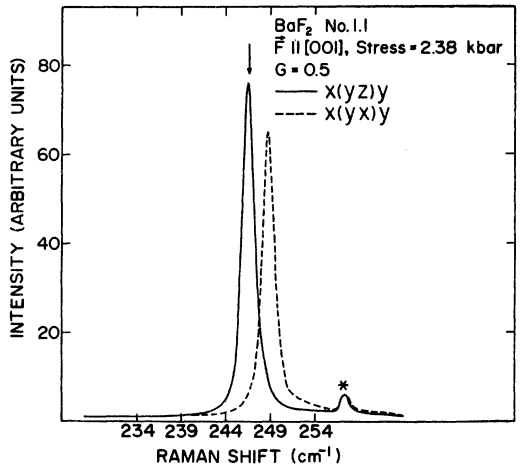

FIG. 8. Polarization characteristics of the stress-induced components in BaF_2 for $\vec{F} \parallel [001]$, at a stress of 2.38 kbar; $T \sim 15$ °K. The arrow denotes the zero-stress position of the line. $\hat{x} \parallel [100]$, $\hat{y} \parallel [010]$, $\hat{z} \parallel [001]$. The calibration line denoted by the asterisk was obtained from a potassium discharge lamp. The wavelength of this line was determined as 4942.10 Å using the plasma line at 4933.24 Å from the Ar^+ laser as reference.

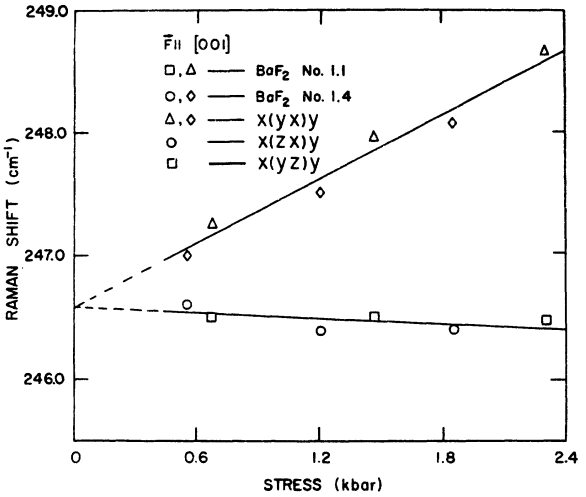

FIG. 9. Positions of the stress-induced components in BaF_2 as a function of the applied stress for $\vec{F} \parallel [001]$. The comments made in the caption of Fig. 7 apply here also.

B. Barium Fluoride

Srivastava *et al.*[12] have reported the Raman-active F_{2g} mode of BaF_2 at 242 cm^{-1} at room temperature and 249 cm^{-1} at 77 °K. In our study, using the calibration line from a neodymium hollow cathode lamp, we have determined the line position at room temperature to be 240.9 ± 0.5 cm^{-1} with a half-width of ~8.5 cm^{-1}. At ~15 °K, the Raman shift was 246.6 ± 0.2 cm^{-1} with a half-width of ~1.6 cm^{-1}. Also, the position of the line at 77 °K is very close to that at ~15 °K. Zero-stress polarization studies for BaF_2 similar to those shown in Fig. 1 established that the line possesses F_{2g} symmetry as expected.

During stress measurements the BaF_2 samples frequently cleaved along the (111) plane either upon cooling or at stresses low in comparison to the maximum used for CaF_2. We have been successful in obtaining satisfactory data for $\vec{F} \parallel [001]$, which are presented in Figs. 8 and 9. Figure 8 shows the singlet and the doublet at a stress of 2.38 kbar. The comments made in the case of CaF_2 for $\vec{F} \parallel [001]$ with respect to the symmetry and polarization of the stress-induced components apply to this case also. In Fig. 9 is shown the position of the singlet and the doublet as a function of applied stress. Using the compliance constants of BaF_2[32] the deformation-potential constants a and b have been obtained from the slopes of the straight lines in Fig. 9 and listed in Table XII.

For both CaF_2 and BaF_2, from the results of the present study the expected rate of shift in the fre-

TABLE XII. Deformation-potential constants of the Raman lines of CaF_2, BaF_2, and $Bi_{12}GeO_{20}$. The constants not applicable to a given line are left blank. Line labels correspond to those in Fig. 10. N.D.—not determined in the present study.

Crystal	Line positions (cm^{-1})	Line label	Deformation-potential constants (cm^{-1} per unit strain) a	b	c	d	e	$\lvert f \rvert$	g
CaF_2	327.3		−1287	−271	−103				
BaF_2	246.6		−785	−281	N.D.				
	124.0	7	−467	−165	−106	~0			
	57.5	2c	−295	−251	24	~0			
$Bi_{12}GeO_{20}$	207.2, 209.0	11a, 11b	−251	−454	84	~0			
	87.2	4a					−139	70	
	67.7	3					−250	87	
	130.2	8					−226	47	
	89.4	4b							−210

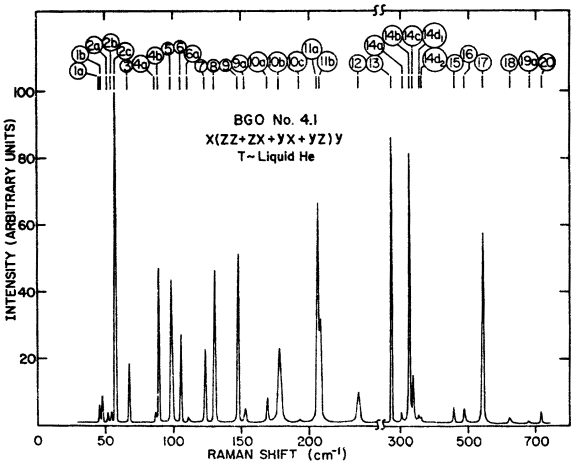

FIG. 10. Raman spectrum of BGO at 15 °K. The spectrum was excited with ~50 mW of circularly polarized 6328-Å radiation from a He-Ne laser. x, y, and z are along the cubic directions. No analyzer was used in the path of the scattered radiation.

quency as a function of applied hydrostatic stress at ~15 °K can be deduced; these are -0.64 cm^{-1}/kbar for CaF_2 and -0.72 cm^{-1}/kbar for BaF_2. The room-temperature hydrostatic shifts measured by Mitra for both crystals[33] are in close agreement with these values.

C. Bismuth Germanium Oxide

The Raman spectrum of $Bi_{12}GeO_{20}$ at ~15 °K is shown in Fig. 10. The experimental conditions under which this spectrum was obtained have been described in an earlier paper.[13] As pointed out before, it is a very rich spectrum consisting of lines of A, E, and F symmetry as well as LO-TO-split F modes.[13] Thus the effect of uniaxial stress on different types of phonons can be examined in this case. We present here the piezospectroscopic results obtained for illustrative cases of each type. The deformation-potential constants for the lines examined are listed in Table XII.

In the present measurements, care was exercised to minimize the depolarization effects arising from optical activity[13] in $Bi_{12}GeO_{20}$. The 6328-Å radiation was used for exciting the spectrum; the sensitivity of the spectrometer in this region is nearly 2.5 times greater for radiation polarized perpendicular to the grating grooves as compared to that polarized parallel to the grooves. Thus a proper comparison of the relative intensities of the stress-induced components with the predicted behavior must include appropriate corrections for the polarization response of the instrument and the depolarizing effects due to optical activity. For $\vec{F} \parallel [110]$, it is seen from Table II that the crystal acquires the monoclinic symmetry C_2. In this case, for linearly polarized radiation propagating at right angles to the C_2 axis, the polarization direction is not affected and continues to be linear. However, linearly polarized radiation propagating along the C_2 axis can emerge elliptically polarized as a result of the photoelastic birefringence in the crystal. Thus for $\vec{F} \parallel [110]$, when the scattered radiation is observed along [001] direction as is the case here, depolarization of scattered radiation can occur owing to stress-induced birefringence in the crystal. The observed results seem to indicate that such effects are not large. Nevertheless, as the spectra reported here are uncorrected for the depolarization effects just mentioned and the polarization response of the spectrometer, we will concern ourselves mainly with the polarization characteristics of the stress-induced components and only qualitative intensity comprisons are made, in general.

The experimental results obtained for the F line at 124.0 cm^{-1} (line 7) with applied force along [111], [110], or [001] are shown in Fig. 11. The zero-stress line is also shown in each case. For $\vec{F} \parallel [111]$, the line is seen to split into two components in the $x''(z''z''+z''x'')y''$ polarization, while only one component is seen in $x''(y''z''+y''x'')y''$. Comparison of these results with the polarization characteristics predicted in Tables IV and VII shows that in the latter polarization only the doublet should appear while in the former, both the doublet and the singlet should be seen. Thus the lower-frequency component is the doublet with E symmetry in the new point group C_3, while the higher-frequency component is the singlet which has A symmetry in C_3. For $\vec{F} \parallel [001]$, two components are seen in $x(yz+yx)y$ polarization. Through separate polarization measurements, it was ascertained that the higher-frequency component is seen

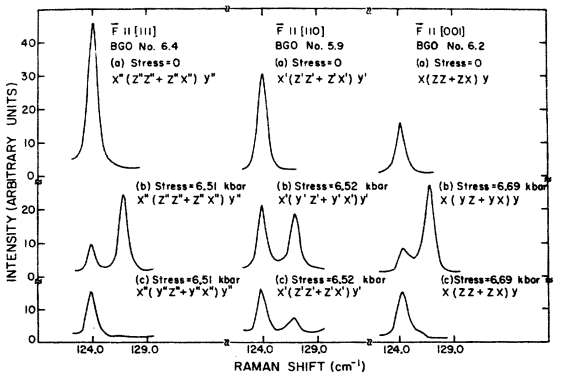

FIG. 11. Stress-induced components of the F mode at 124.0 cm^{-1} (line 7) in BGO for $\vec{F} \parallel [111]$, [110], and [001]. The zero-stress spectrum is also shown in each case; $T \sim 15$ °K. The crystallographic orientations are the same as for Fig. 7 except that $x'' \parallel [11\bar{2}]$, $y'' \parallel [110]$.

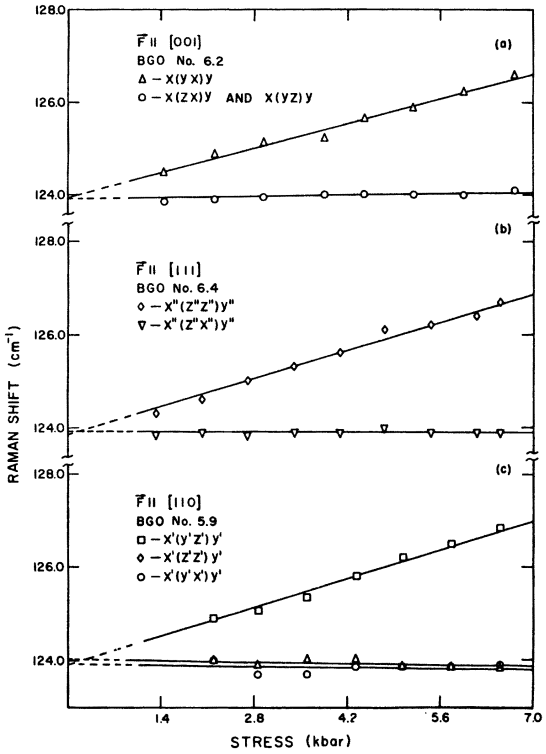

FIG. 12. The positions of the stress-induced components of the 124.0-cm^{-1} line as a function of the applied stress. The crystallographic orientations are the same as for Fig. 11. The comments made in the caption of Fig. 7 apply here also.

only in $x(yx)y$, while the other component has the $x(yz)y$ polarization. Hence they have B_1 and B_3 symmetry, respectively, in the new point group D_2. In $x(zz+zx)y$ polarization a single component is observed and thus it belongs to B_2 symmetry in D_2. The position of this component, within experimental accuracy, is the same as that seen in $x(yz)y$. From Eqs. (16) we note that such a coincidence can occur if $d \simeq 0$ for a given F mode and hence its behavior for $\vec{F} \parallel [001]$ simulates that of the F_{2g} mode in O_h.

For $\vec{F} \parallel [110]$, from Table II it is seen that the F mode splits into three components in the point group C_2. From Tables IV and X we note that a single component with A symmetry should be seen in $x'(z'z'+z'x')y'$ polarization while two components with B symmetry will be seen in the $x'(y'z'+y'x')y'$. The observed results are consistent with this expectation. It is felt that the weaker component seen in $x'(z'z'+z'x')y'$ is due to spillover from the forbidden B-symmetry line at that frequency. It was noticed that within experimental accuracy the component with A symmetry has the same frequency as one of the lines with B symmetry. It can be shown that this is a consequence of the specific values of the deformation-potential constants a, b, c, and d associated with this F mode.

Figure 12 shows the variation in the frequency of the stress-induced components as a function of the magnitude of the applied stress for $\vec{F} \parallel [001]$, [111], or [110]. The straight lines represent linear least-squares fit to the data points in each case. From the slopes of the lines, the deformation-potential constants can be determined using Eqs. (7), (16), and (17) as well as the compliance constants of $Bi_{12}GeO_{20}$. As the low-temperature elastic constants of $Bi_{12}GeO_{20}$ have not been determined, we use their known values at room temperature[34] in calculating the deformation-potential constants of all the lines examined in this study.

We have also examined the behavior of the sharp, intense, triply degenerate mode at 57.5 cm^{-1} (line 2c) under uniaxial stress along the three crystallographic directions previously mentioned. The magnitudes of the splittings were generally $\lesssim 1.2$ cm^{-1} at the highest stresses used in this study. The polarizations of the stress-induced components were in agreement with the behavior described already for the F mode at 124.0 cm^{-1}. The deformation-potential constants of the 57.5-cm^{-1} line are listed in Table XII.

The effect of uniaxial stress along [111], [110], or [001] on the TO-LO pair at 207.2 and 209.0 cm^{-1}, respectively, (lines 11a and 11b) is shown in Fig. 13. (Note that the position of these lines was given before[13] as 207.0 and 208.5 cm^{-1}, respectively. The present values are based on improved statistics.) The zero-stress spectrum is also shown in each case. Figure 14 shows the positions of the stress-induced components of the TO-LO pair as a function of the magnitude of the applied stress for the three crystallographic di-

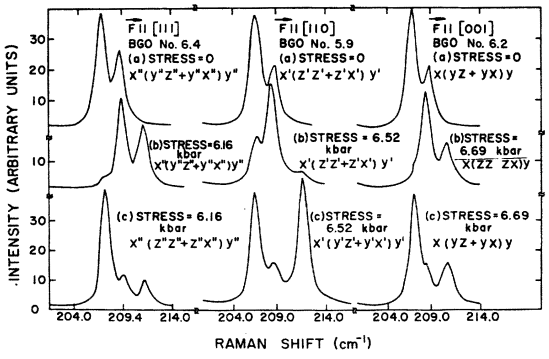

FIG. 13. Stress-induced components of the LO-TO-split F mode at 207.2 cm^{-1} (TO) and at 209.0 cm^{-1} (LO) (lines 11a and 11b) in BGO for $\vec{F} \parallel$ [111], [110], and [001]. The zero-stress spectrum is also shown in each case; $T \sim 15$ °K. The crystallographic orientations are the same as for Fig. 11.

rections. It is seen that for all three directions of applied force, three components are observed and in each case the highest-frequency component can be identified as the stress-shifted LO mode. The remaining two components are evidently the stress-induced components of the TO line. In Fig. 13, for $\vec{F} \parallel [111]$, two components are seen in $x''(y''z'' + y''x'')y''$ polarization. As only the doublet should appear in this polarization, we conclude that the two lines correspond to $(TO)_\perp$ and LO, which constitute the doublet in this case. In $x''(z''z'' + z''x'')y''$ polarization, in addition to the doublet, the singlet also should be seen. Thus the strong component seen in this case is the singlet which corresponds to $(TO)_\parallel$. For $\vec{F} \parallel [001]$, the stress-induced TO component at the lower frequency is seen as the strongest line in $x(yz+yx)y$ polarization, whereas the TO component at the higher frequency is the strongest line in $x(zz+zx)y$. Under stress, the TO component seen distinctly in $x(zz + zx)y$ appears much weaker in $x(yz+yx)y$ and vice versa. Hence the TO component in the former case must have $x(zx)y$ polarization and thus its energy shift under stress is described by the eigenvalue λ_2 in Eq. (16). It was ascertained from a separate polarization measurement that under stress the lower-frequency TO component seen in $x(yz+yx)y$ polarization has $x(yx)y$ polarization and hence its shift under stress is described by λ_3 in Eqs. (16). As the two stress-induced components of the TO line belong to λ_2 and λ_3, the stress-shifted LO mode is expected to belong to λ_1; indeed the polarization study of this mode indicated that it has a higher intensity in $x(yz)y$ than in $x(zx)y$.

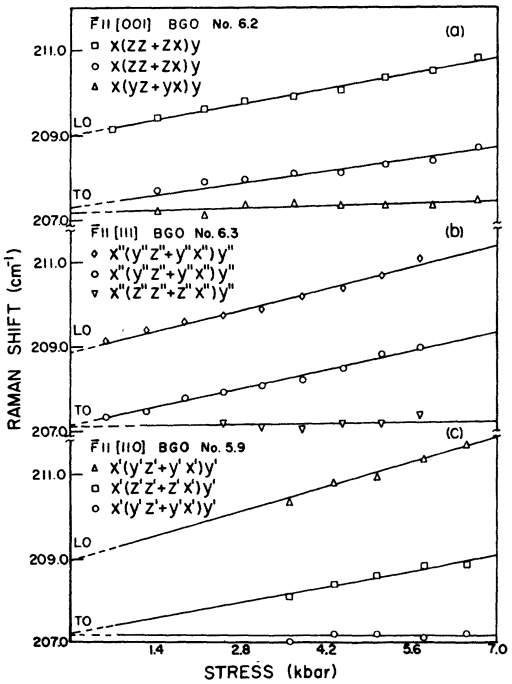

FIG. 14. The positions of the stress-induced components of the LO–TO pair as a function of the applied stress. The crystallographic orientations are the same as for Fig. 11. The comments made in the caption of Fig. 7 apply here also.

As discussed in the case of the triply degenerate F mode at 124.0 cm^{-1}, for $\vec{F} \parallel [110]$, two components should be seen in $x'(y'z'+y'x')y'$ polarization while a single component should be seen in $x'(z'z' + z'x')y'$. Thus we conclude that in Fig. 13, the strong TO component and the stress-shifted LO mode seen in $x'(y'z'+y'x')y'$ have B symmetry while the strong central component in $x'(z'z' + z'x')y'$ has A symmetry in C_2. It is felt that the weaker central component in $x'(y'z'+y'x')y'$ arises from spill-over of the A-symmetry line at that position. Similarly in $x'(z'z'+z'x')y'$, the weaker lines on either side of the strong central component are attributed to spill-over from the two lines of B symmetry.

It is worth noting in Fig. 14 that for $\vec{F} \parallel [111]$, $(TO)_\perp$ and LO shift at the same rate as a function of the stress. Thus we conclude that the LO-TO splitting remains constant up to the highest stresses used in this study. From the polarization features of the stress-induced components, the appropriate eigenvalue can be assigned in each case from Eqs. (7), (16), and (17), and the slopes of the straight lines in Fig. 14 can be used to determine the deformation-potential constants of this LO-TO-split F mode.

We will now discuss the effects of uniaxial stress on the nondegenerate (A) and double-degenerate (E) lines we have investigated. In the present study, the observed splitting of the E modes as a function of applied stress, for $\vec{F} \parallel [001]$ or [110], has been used to determine e and $|f|$, and these are listed in Table XII. However, owing to the depolarizing effects already discussed, no attempt has been made to correlate the observed intensities of the stress-induced components of the E modes for either of the above two directions of applied force, in order to obtain u and $|v|$.

The behavior of the E mode at 87.2 cm^{-1} (line 4a)[35] and the A mode at 89.4 cm^{-1} (line 4b) for $\vec{F} \parallel [001]$, [110], or [111] is shown in Fig. 15 together with the zero-stress spectra. The intense A mode is shown truncated in all cases. The arrows denote the zero-stress positions. It is seen from Eq. (25) that the energy shift of a given A mode must be isotropic with respect to the crystallographic direction of the applied force. For all three directions of applied force this was found to be true, within experimental accuracy, for the A mode at 89.4 cm^{-1}. In addition, it was noticed that the intensity of this A line decreases with increasing stress. Such a stress-dependent intensity

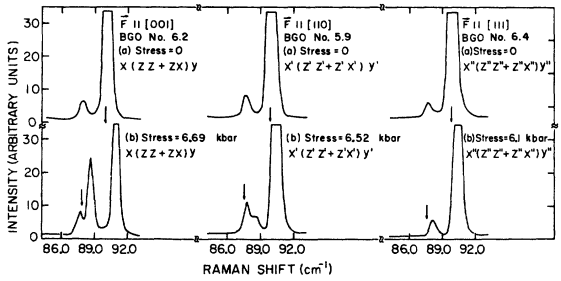

FIG. 15. Stress-induced components of the E mode at 87.2 cm^{-1} (line 4a) and the stress-shifted A mode at 89.4 cm^{-1} (line 4b) for $\vec{F} \parallel [001]$, [110], and [111]. The zero-stress spectrum is also shown in each case. The intense A mode is shown truncated in all cases; $T \sim 15$ °K. The crystallographic orientations are the same as for Fig. 11.

change is not expected on the basis of the deformation-potential approach discussed in Sec. III.

For $\vec{F} \parallel [001]$ or [110] it is seen that the E mode at 87.2 cm^{-1} splits into two components as expected from Table II and Eqs. (20) and (21). Also, for $\vec{F} \parallel [111]$, the E mode merely shifts under the stress and remains degenerate as expected. The polarization characteristics of the stress-induced components in Fig. 15 are in agreement with those predicted in Tables IV and XI. Both for $\vec{F} \parallel [001]$ and [110], the total intensity in the two stress-induced components is greater than that at zero stress. This is contrary to the conclusion derived in this respect from Eq. (22) and Table XI. In addition, it was noted in Sec. III that the pattern of relative intensities of the two stress-induced components should be similar for $\vec{F} \parallel [001]$ and [110]. However, the observed pattern of relative intensities for $\vec{F} \parallel [001]$ is found to be opposite to that for $\vec{F} \parallel [110]$. It is felt that the prediction of relative intensities given in Eqs. (23) and (24) may not be applicable to the present case where pronounced enhancement of intensity occurs.

The effect of uniaxial stress along the [001] direction on two of the E modes at 67.7 (line 3) and 130.2 cm^{-1} (line 8) is shown in Fig. 16. It should be noted that at zero stress, there is a very weak Raman line at 66.7 cm^{-1}. This feature was not detected in our earlier work[13] and was observed during the present study because of the higher resolution and improved signal-to-noise ratio attained. The intensity of this weak feature was found to increase with increasing stress in addition to a shift in its peak position, for both $\vec{F} \parallel [001]$ and [110]. Following its position as a function of stress, we identify the component at the lowest frequency in the presence of the stress as arising from this feature. Polarization study of this line indicates that it is most likely of A symmetry. The two higher-frequency components by the side of this line represent the stress-induced components of the E mode at 67.7 cm^{-1}. The observed polarization characteristics of the two components are consistent with those predicted in Tables IV and XI. At zero stress, the asymmetry of the 130.2-cm^{-1} line on the higher-frequency side arises from the weaker F mode[13] at 131.2 cm^{-1}. Hence the stress-induced components of the E mode were clearly observed in the $x(zz)y$ polarization which eliminates overlap from the neighboring F mode. As in the case of the E mode at 67.7 cm^{-1}, the polarization of the stress-induced components in this case is consistent with the expected behavior.

We have also examined the behavior of the other A lines at 148 (line 9), 272 (line 13), and 542.6 cm^{-1} (line 17) under uniaxial stress. The observed rates of shift as a function of stress for these lines were comparable to that reported here for the A mode at 89.4 cm^{-1} (line 4b).

It should be mentioned that Bairamov *et al.*[36] have recently reported a uniaxial-stress study of the Raman spectrum of $Bi_{12}GeO_{20}$ at room temperature, using a compressive stress of 8×10^7 dyn/cm^2 along an unspecified crystallographic direction; this stress is nearly two orders of magnitude lower than the maximum stresses used in the present study. Thus, they have not observed any splittings of degenerate modes nor have they reported any polarization measurements. However, they have reported *negative* shifts for the lines at 89, 146, and 272 cm^{-1}, the shifts being 1, 3, and 4 cm^{-1}, respectively. From our earlier study[13] we identify all three lines as A modes though Bairamov *et al.*[37]

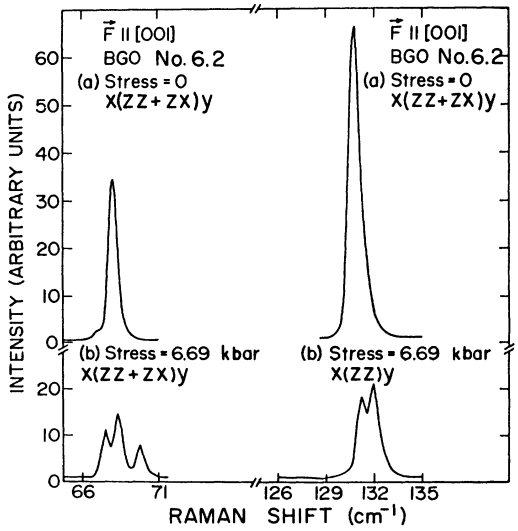

FIG. 16. Stress-induced components of the E modes at 67.7 cm^{-1} (line 3) and at 130.2 cm^{-1} (line 8) for $\vec{F} \parallel [001]$; $T \sim 15$ °K. The zero-stress spectra are also shown. x, y, and z are along the cubic directions.

have assigned only the 146-cm^{-1} line as A mode and the other two are incorrectly assigned as E modes. In our present study using compressive stress, we observed *positive* shifts of these three A lines with the shifts not exceeding ~1 cm^{-1} at ~7×10^9 dyn/cm^2. Thus we feel that the "stress-induced" shifts reported by Bairamov *et al.*[36] may reflect their accuracy in determining the line position.

V. CONCLUSIONS

The present investigation shows that the low-temperature piezospectroscopic study of Raman spectra of crystals in a useful technique in the study of lattice vibrations; it enables the determination of their symmetries and the associated deformation-potential constants. For all the lines studied, the number of stress-induced components and their polarization features have provided independent confirmation of the line symmetry known from previous zero-stress studies.[11,13] From Table XII it is seen that there is a variation in the magnitude as well as the sign of the deformation-potential constants for the different lines studied. Such information should prove useful in any attempt to correlate these constants with changes in the interatomic force constants arising from the lattice deformation caused by the applied force.

It should be noted that the relative positions of the stress-induced components for $\vec{F} \parallel [001]$ are determined by the relative magnitude and sign of the constants a and b as well as the compliance constants s_{11} and s_{12}. For all three crystals studied here, $(s_{11}-s_{12})$ is positive. For both CaF_2 and BaF_2 the singlet has a higher frequency than the doublet for $\vec{F} \parallel [001]$, whereas for Si[8] and Ge,[9] which also have a positive $(s_{11}-s_{12})$, the converse is true. This is reflected in the fact that $(a-b)$ is positive for Si and Ge while it is negative for both CaF_2 and BaF_2. For $\vec{F} \parallel [111]$, the singlet has a higher frequency than the doublet in all four crystals, yielding a negative sign for c since s_{44} is positive for all of them. In a similar manner, the magnitudes and signs of the constants in Table XII for the lines in $Bi_{12}GeO_{20}$ account for the relative positions of the stress-induced components. It is also interesting to note that in the two triply degenerate and the LO-TO-split F modes investigated in $Bi_{12}GeO_{20}$, $d \sim 0$, though it can be nonzero for the point group T. This might indicate that these modes have an inherently higher symmetry than is generally permissible in T.

While the values of b for CaF_2 and BaF_2 are comparable, the value of a for BaF_2 is nearly 60% of that for CaF_2. This substantial difference is of interest from a lattice dynamical viewpoint. For Si and Ge, Cerdeira *et al.*[9] have attempted a comparison of the experimental values of a, b, and c with theoretical values determined from models containing explicit contributions to the internal energy of each unit cell from bond-bending and bond-stretching forces in the presence of the applied force. They conclude that the agreement is not completely satisfactory for any of the models considered. The lattice dynamics of crystals with the fluorite structure has been the subject of several experimental and theoretical studies in the past. The second-order Raman spectra of fluorites[38] has been recently studied. In addition, inelastic neutron scattering studies on CaF_2[39] and BaF_2[40] have enabled a determination of the shell-model parameters in the lattice dynamics of both crystals. Using the known elastic and optical properties of CaF_2, Srinivasan[41] and Ganesan and Srinivasan[42] have determined the force constants associated with the ionic interactions in the rigid-ion approximation. The short-range force constants of CaF_2, BaF_2, and SrF_2 have also been evaluated by Axe[43] using the shell-model approach. Thus, in view of the relative simplicity of the fluorite structure and the available information on the dynamics of CaF_2 and BaF_2, it should be of interest to relate the observed deformation-potential constants for both crystals to the changes in the force constants arising from the lattice distortion due to the applied force.

ACKNOWLEDGMENTS

The authors wish to express their thanks to Professor S. Rodriguez for many stimulating discussions and consultations, and to Professor H. J. Yearian and Miss Louise Roth for their help in orienting and preparing the samples used in the present work. Thanks are due to V. J. Tekippe for help in the use of the quantitative stress cryostat.

---

†Work supported by the National Science Foundation (GH 32001 and MRL Program No. GH 33574) and the Advanced Research Projects (IDL Program No. DAHC-0213).

[1]I. Balslev, in *Semiconductors and Semimetals*, edited by R. K. Willardson and A. C. Beer (Academic, New York, 1972), Vol. 9, p. 403.

[2]P. Fisher and A. K. Ramdas, in *Physics of the Solid State*, edited by S. Balakrishna, M. Krishnamurthi, and B. Ramachandra Rao (Academic, New York, 1969), p. 149.

[3]I. Balslev, Phys. Rev. **143**, 636 (1966).

[4]G. S. Hobson and E. G. S. Paige, Proc. Phys. Soc. Lond. **88**, 437 (1966).

[5]I. G. Nolt and A. J. Sievers, Phys. Rev. **174**, 1004 (1968); W. Hayes, H. F. Macdonald, and R. J. Elliott, Phys. Rev. Lett. **15**, 961 (1965).

[6]M. Marieé and J. P. Mathieu, C.R. Acad. Sci. (Paris) **223**, 147 (1946).

[7]V. J. Tekippe and A. K. Ramdas, Phys. Lett. A **35**, 143 (1971); V. J. Tekippe, A. K. Ramdas, and S. Rodriguez, in Proceedings of the Third International Conference on Raman

Spectroscopy, Reims, France, 1972 (unpublished).
[8]E. Anastassakis, A. Pinczuk, E. Burstein, F. H. Pollak, and M. Cardona, Solid State Commun. **8**, 133 (1970).
[9]F. Cerderia, C. J. Buchenauer, F. H. Pollak, and M. Cardòna, Phys. Rev. B **5**, 580 (1972).
[10]A brief report is given in S. Venugopalan and A. K. Ramdas, Bull. Am. Phys. Soc. **18**, 75 (1973).
[11]L. Couture and J. P. Mathieu, C.R. Acad. Sci. (Paris) **224**, 1217 (1947).
[12]R. S. Krishnan and P. S. Narayanan, Indian J. Pure Appl. Phys. **1**, 196 (1963). See also, R. Srivastava, H. V. Lauer, Jr., L. L. Chase, and W. E. Bron, Phys. Lett. A 36, 333 (1971).
[13]S. Venugopalan and A. K. Ramdas, Phys. Rev. B **5**, 4065 (1972).
[14]Harshaw Chemical Co., Crystal Solid State Department, 1945 E. 97th St., Cleveland, Ohio 44106.
[15]Isomet Corp., 103 Bauer Drive, Oakland, N.J. 07436.
[16]V. J. Tekippe, H. R. Chandrasekhar, P. Fisher, and A. K. Ramdas, Phys. Rev. B **6**, 2348 (1972).
[17]A. A. Ballman, J. Cryst. Growth **1**, 37 (1967).
[18]P. V. Lenzo, E. G. Spencer, and A. A. Ballman, Appl. Opt. **5**, 1688 (1966).
[19]A. Feldman, W. S. Brower, Jr., and D. Horowitz, Appl. Phys. Lett. **16**, 201 (1970).
[20]Manufactured by Osram Co., Berlin, Germany. The calibration wavelengths are taken from *Handbook of Chemistry and Physics*, 43rd ed., edited by C. D. Hodgman (Chemical Rubber Publishing Co., Cleveland, 1961), p. 2929.
[21]Westinghouse Electric Corp., Electronic Tube Division, Elmira, N.Y. 14902. The calibration wavelength was taken from the source cited in Ref. 20, p. 2916.
[22]H. S. Peiser, J. B. Wachtman, Jr., and R. W. Dickson, J. Res. Natl. Bur. Stand. (U.S.) A **67**, 395 (1963).
[23]A. A. Kaplyanskii, Opt. Spektrosk. **16**, 1031 (1964) [Opt. Spectrosc. **16**, 557 (1964)].
[24]S. Rodriguez, P. Fisher, and F. Barra, Phys. Rev. B **5**, 2219 (1972). In the present paper we follow the approach outlined in this reference.
[25]E. P. Wigner, *Group Theory and its Application to the Quantum Mechanics of Atomic Spectra* (Academic, New York, 1959), Sec. 4, p. 115.
[26]See, also, S. Ganesan, A. A. Maradudin, and J. Oitmaa, Ann. Phys. (N.Y.) **56**, 556 (1970); E. Anastassakis and E. Burstein, J. Phys. Chem. Solids **32**, 313 (1971); J. Phys. Chem. Solids **32**, 563 (1971). These authors have arrived at the secular equation in Refs. 23 and 24 by starting with the dynamical matrix; it can be shown that the two procedures are equivalent.
[27]J. F. Nye, *Physical Properties of Crystals* (Oxford U. P., Oxford, England, 1964).
[28]See Ref. 27, p. 92.
[29]R. Loudon, Adv. Phys. **13**, 423 (1964).
[30]This is an assumption which has to be verified experimentally. See, for example, Ref. 9, where it is found that this is true for the III-V compounds investigated, but not for the II-VI compound ZnSe.
[31]D. R. Huffman and M. H. Norwood, Phys. Rev. **117**, 709 (1960). The elastic constants given here for 4.2 °K have been used by us. The elastic constants do not vary strongly with temperature and the changes between 4.2 and ≈15 °K are neglected.
[32]D. Gerlich, Phys. Rev. **135**, 1331 (1964); we use the elastic constants given here extrapolated to 0 °K. See comment under Ref. 31.
[33]The unpublished results of S. S. Mitra are quoted by J. R. Ferraro, H. Horan, and A. Quattrochi, J. Chem. Phys. **55**, 664 (1971). We have assumed that Mitra has taken compressive hydrostatic stress to be positive in sign.
[34]M. Onoe, A. W. Warner, and A. A. Ballman, IEEE Trans. Sonics Ultrason. **14**, 165 (1967).
[35]Due to a typographical error, the position of this line is incorrectly given as 97.2 cm^{-1} in Table V of Ref. 13.
[36]B. Kh. Bairamov, B. P. Zakharchenya, and Z. M. Khashkhozhev Fiz. Tverd. Tela **14**, 1374 (1972) [Sov. Phys.-Solid State **14**, 1181 (1972)].
[37]B. Kh. Bairamov, B. P. Zakharchenya, R. V. Pisarev, and Z. M. Khashkhozhev, Fiz. Tverd. Tela **13**, 3366 (1971) [Sov. Phys.-Solid State **13**, 2827 (1972)].
[38]N. Krishnamoorthy and V. Soots, Can. J. Phys. **50**, 1350 (1972).
[39]M. M. Elcombe and A. W. Pryor, J. Phys. C **3**, 492 (1970).
[40]J. P. Hurrell and V. J. Minkiewicz, Solid State Commun. **8**, 463 (1970).
[41]R. Srinivasan, Proc. Phys. Soc. Lond. **72**, 566 (1958).
[42]S. Ganesan and R. Srinivasan, Can. J. Phys. **40**, 74 (1961).
[43]J. D. Axe, Phys. Rev. **139**, 1215 (1965).

PHYSICAL REVIEW B VOLUME 8, NUMBER 2 15 JULY 1973

Resonant Second-Harmonic Generation in the Exciton Region of CuCl and ZnO†

D. C. Haueisen* and H. Mahr
Laboratory of Atomic and Solid State Physics, Cornell University, Ithaca, New York 14850
(Received 10 January 1973)

Using a pulsed tunable dye laser pumped by a Q-switched ruby laser, the frequency dependence of second-harmonic generation has been measured in the region of the first and second 1s excitons of CuCl from about 3.18 to 3.34 eV and the region of the C exciton of ZnO from about 3.38 to 3.48 eV. From the data, the frequency dependence of the optical nonlinear susceptibility has been determined using linear optical constants calculated by a Kramers-Krönig analysis of reflectivity. The results for the single nonzero term of the nonlinear susceptibility of CuCl and the two terms d_{zzz} and d_{zxx} of ZnO have been fit theoretically by an anharmonic-oscillator model employing two oscillators.

I. INTRODUCTION

The intent of the work described here was to experimentally measure the frequency dependence of optical-second-harmonic generation and then to deduce from the data the frequency dependence of the nonlinear optical susceptibility. The measurements were made for second-harmonic light gen-